Aalborg Universitet

Analysis of Simulated and Measured Indoor Channels for mm-Wave Beamforming Applications

Karstensen, Anders; Fan, Wei; Zhang, Fengchun; Nielsen, Jesper Ødum; Pedersen, Gert F.

Research Article

Analysis of Simulated and Measured Indoor Channels for mm-Wave Beamforming Applications

Anders Karstensen [ID]**, Wei Fan** [ID]**, Fengchun Zhang, Jesper Ø. Nielsen, and Gert F. Pedersen**

Antennas, Propagation and Millimetre-Wave Systems at the Department of Electronic Systems, Faculty of Engineering and Science, Aalborg University, Aalborg, Denmark

Correspondence should be addressed to Anders Karstensen; andka@es.aau.dk

Ray tracing- (RT-) assisted beamforming, where beams are directly steered to dominant paths tracked by ray tracing simulations, is a promising beamforming strategy, since it avoids the time-consuming exhaustive beam searching adopted in conventional beam steering strategies. The performance of RT-assisted beamforming depends directly on how accurate the spatial profiles of the radio environment can be predicted by the RT simulation. In this paper, we investigate how ray tracing-assisted beamforming performs in both poorly furnished and richly furnished indoor environments. Single-user beamforming performance was investigated using both single beam and multiple beams, with two different power allocation schemes applied to multibeamforming. Channel measurements were performed at 28–30 GHz using a vector network analyzer equipped with a biconical antenna as the transmit antenna and a rotated horn antenna as the receive antenna. 3D ray tracing simulations were carried out in the same replicated propagation environments. Based on measurement and ray tracing simulation data, it is shown that RT-assisted beamforming performs well both for single and multibeamforming in these two representative indoor propagation environments.

1. Introduction

Utilization of millimeter-wave (mm-wave) frequencies for 5G standards has gained considerable interest within the wireless industry in recent years [1, 2]. The reasons can be attributed to the vast available bandwidth and its potential for enabling the implementation of massive antenna arrays both at the base station and mobile terminal sides. Standardization work of 5G specifications is ongoing in the Third Generation Partnership Project (3GPP) [3].

To enable 5G cellular systems at mm-wave bands, two challenges must be addressed: coverage for a sufficiently large area and support both for line-of-sight (LOS) and non-LOS scenarios where the direct LOS path between the transmitter (Tx) and the receiver (Rx) is not present [2, 4]. Beamforming at mm-wave bands is seen as an enabling technique to fulfill these two requirements [4, 5], since highly directive arrays can be steered in various angles to compensate for propagation losses and to achieve significant system capacity and throughput gains [4, 5].

Accurate knowledge of spatial channels at mm-wave bands is essential for assessing beamforming performance [6, 7]. Extensive mm-wave channel measurement campaigns have been performed recently, see, for example, [8, 9]. Channel sounding measurement is expensive, which is the case especially at mm-wave bands. Hardware equipment for mm-wave channel sounding is more costly and might be even commercially unavailable. Furthermore, extensive channel sounding in various propagation scenarios at many potential mm-wave frequency bands is time-consuming, though extensive efforts are ongoing. The ray tracing (RT) method has been used as an alternative to obtain radio propagation channels for frequency bands below 6 GHz [10]. RT simulation is expected to be suitable to predict mm-wave multipath channels, due to the more ray-optical behaviour at mm-wave bands. RT simulations were conducted in many studies to assess coverage, large-scale parameters, and multipath effects at mm-wave bands in various propagation environments [8]. A preliminary overview of the 5G channel propagation phenomena and channel models for bands up

to 100 GHz was reported in [8], where the results were derived based on extensive channel sounding measurements and RT simulations when measurement results were not available. The METIS map-based model, which was proposed to fulfill the 5G channel modeling requirements, is based on the 3D RT principle as well [11]. A few studies validating RT simulations, via comparing RT simulation results with channel measurements at 60 GHz, were reported in the literature [12–15]. In [12], measurements in a conference room are compared to a detailed model in RT. The RT tool does not include scattering, and the RMS delay-spread power and RMS delay-received power are underestimated but show good agreement for the most dominant paths. In [13, 14], a RT tool including diffuse scattering is calibrated and used to compare RT to measurements in a furnished but open indoor environment. By including diffuse scattering in RT simulations, the agreement with measurement improves on path loss, delay spread, and angular spread. In [15], an indoor office is measured and replicated in a RT tool. A Tx antenna placed in a corner sweeps $0°$ to $90°$ in azimuth and $30°$ to $−60°$ in elevation. The authors utilize RT to identify clusters for different Tx-Rx polarization and measurements to tune the RT scattering parameters.

Comprehensive comparison of RT simulations with measurements at other mm-wave bands, however, is quite limited. In [16], the dynamic channel characteristics are investigated by measurement and simulation at 23.5 GHz in a conference room environment. The paths are tracked in terms of delay and angle parameters to determine life duration of the paths. The duration of most paths is within 5 m, but LOS and strong reflections live much longer. The paper reports strong correlation of the spatial parameters between measurement and RT, supporting the feasibility of developing beam tracking algorithms for dominant paths. In [17], measurements at 45 GHz from an indoor conference scenario are compared with RT and good agreement with strong components is reported.

Recently, an idea named RT-assisted beamforming was proposed [6, 7], which can be used as an alternative to beamforming strategies based on extensive search. With conventional beamforming strategies, for example, beamforming training in the 802.11ad standard [18], extensive beam search is required both at the Tx and Rx side, which can be very time-consuming. A beamforming prototype for 5G mm-wave systems was presented in [4], which reported a beam training time of 45 ms. However, the search range was limited to 60 degrees in the horizontal plane with a half power beam width (HPBW) of 10 degrees. An extension to full 3D with very narrow beams of a few degrees could arguably increase the beam searching time to several hundreds of milliseconds.

The basic idea of RT-assisted beamforming is that multiple beams can be steered directly to the dominant directions predicted by the RT tool, thus avoiding the need of exhaustive beam searching [6], but requires knowledge of the terminal position. RT-assisted beamforming is interesting at mm-wave bands, since conventional exhaustive beam searching technique can be slow, especially when multiple narrow beams (e.g., pencil beam) are available with a massive number of array elements at the mm-wave bands [6]. RT was proposed as a real-time prediction tool to assist beamforming strategies due to its short-path tracking time [6]. In [6, 7], RT simulations alone were used to evaluate advanced pencil-beamforming techniques in terms of carrier-to-interference plus noise ratio and throughput density in a reference indoor multiuser environment. In [19], multiple users and base stations are simulated at 73 GHz in a crowded urban environment. RT identifies secondary beam alignment in the case of blockage of the current beam alignment. The best beam alignment through multiple moving obstacles is continuously updated, increasing link quality and reducing outage probability.

While there have been previous investigations on RT-assisted beamforming [6, 7, 19], the performance analysis was restricted to simulated channels only. To bring this idea to practice, we must first investigate the feasibility of acceptable performance under different propagation scenarios, both simulated and measured ones, where any discrepancies between the simulation and measurement will translate to a deviation from the maximum achieved beamforming performance. However, to the best knowledge of the authors, no such work has been reported in the literature. In an attempt to answer these questions, an extensive multidimensional analysis of measured and RT-simulated channels at 28–30 GHz is presented in the paper. The analysis was performed both in LOS and non-LOS scenarios in two different indoor environments, one poorly furnished and one richly furnished, respectively. The performance of the RT-assisted beamforming technique is then assessed for a uniform circular array (UCA), utilizing the measured and RT-simulated channels.

In Section 2, the basic idea of RT-assisted beamforming and principle of multibeam steering is briefed. After that, an extensive multidimensional analysis of the measured and RT-simulated channels is detailed in Section 3. In Section 4, the performance of the RT-assisted beamforming technique is evaluated, based on the measured and simulated channels. Section 5 concludes the paper.

2. RT-Assisted Beamforming

The principle of RT-assisted beamforming is illustrated in Figure 1. Basically, a RT simulation is firstly performed to determine the power angular spectrum of the propagation channel. The antenna array elements are then properly weighted to steer beams towards the major paths identified in the RT simulation. Multibeam steering can be realized, via steering beams towards major directions simultaneously.

In this paper, a UCA will be used to evaluate the beamforming performance when using the RT-assisted beamforming in actual channels that may differ from those predicted by the ray tracing. A UCA is illustrated in Figure 2 with N elements and radius r for incoming path k with respect to the array center. Assuming that the channel impulse response (CIR) between the transmitter and the center of the array consists of K plane waves, the channel frequency response is
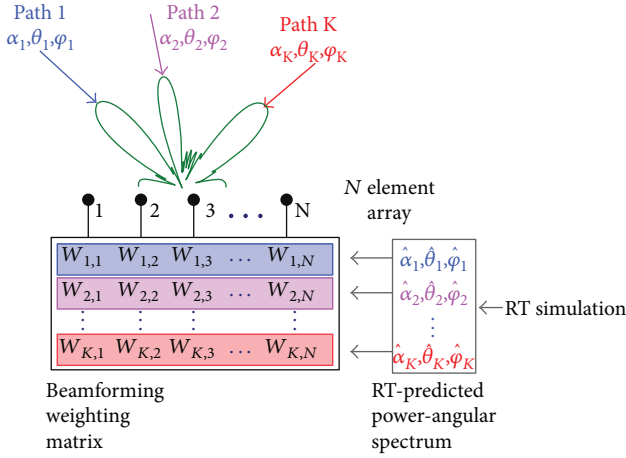
FIGURE 1: An illustration of the RT-assisted beamforming principle. The spatial channel consists of K paths, with its kth path characterized by its amplitude α_k, azimuth angle ϕ_k and elevation angle θ_k with $k \in [1, K]$.
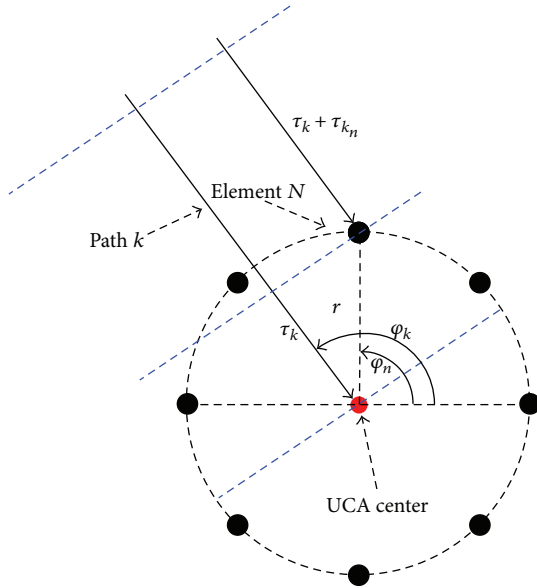

FIGURE 2: UCA with radius r and N elements for the incoming path k.

$$H(f) = \sum_k \alpha_k \cdot \exp(-j2\pi f \tau_k), \tag{1}$$

where α_k and τ_k denote the complex amplitude and delay, respectively, of the kth path and f is the carrier frequency. The kth path with azimuth and elevation angles ϕ_k and θ_k arrives at the nth array element with delay τ_{k_n} with respect to the array center

$$\tau_{k_n} = -\frac{r \cdot \sin(\theta_k) \cdot \cos(\phi_n - \phi_k)}{c}, \tag{2}$$

where c is the speed of light and $\phi_n = 2\pi n/N$. Elevation angles are measured from the z-axis, and azimuth angles are measured counterclockwise from the x-axis on the xy plane. The frequency response of the nth element can be written as

$$H_n(f) = \sum_k a_k \cdot \exp\left[-j2\pi f\left(\tau_k + \tau_{k_n}\right)\right]. \tag{3}$$

Assuming perfect channel equalization (i.e., realignment of delay and cophasing for all paths [6]), the frequency response matrix of the K paths for a UCA with N antenna elements is

$$\mathbf{H} = \begin{bmatrix} \gamma_{1,1} & \cdots & \gamma_{1,K} \\ \vdots & \ddots & \vdots \\ \gamma_{N,1} & \cdots & \gamma_{N,K} \end{bmatrix} \begin{bmatrix} \alpha_1 \\ \vdots \\ \alpha_K \end{bmatrix}, \tag{4}$$

where we have

$$\gamma_{n,k} = \exp\left[-j2\pi f \frac{r}{c} \sin(\theta_k) \cos(\phi_k - \phi_n)\right]. \tag{5}$$

The array response can be expressed as

$$H_{\text{UCA}} = \begin{bmatrix} \sum_k w_{k,1} \\ \vdots \\ \sum_k w_{k,N} \end{bmatrix}^T \cdot \mathbf{H}, \tag{6}$$

where $()^T$ denotes the transpose operator and $\sum_k w_{k,n}$ represents the summed weights of the K paths for the nth element.

Applying the well-known delay-and-sum beamformer, we have

$$w_{k,n} = \sqrt{\frac{p_k}{N}}(\gamma_{n,k})^*, \tag{7}$$

where $()^*$ denotes the conjugation. p_k is the power allocated to the kth path for the UCA, and we have $p = \sum_{k=1}^K p_k$ with p being the total transmit power.

Equation (6) can be further simplified as

$$
\begin{aligned}
H_{\text{UCA}} &= \begin{bmatrix} \sum_k w_{k,1} \\ \vdots \\ \sum_k w_{k,N} \end{bmatrix}^T \cdot \begin{bmatrix} \gamma_{1,1} & \cdots & \gamma_{1,K} \\ \vdots & \ddots & \vdots \\ \gamma_{N,1} & \cdots & \gamma_{N,K} \end{bmatrix} \begin{bmatrix} \alpha_1 \\ \vdots \\ \alpha_K \end{bmatrix} \\
&= \begin{bmatrix} \sum_n \gamma_{n,1} \cdot \left(\sum_k w_{k,n}\right) \\ \vdots \\ \sum_n \gamma_{n,K} \cdot \left(\sum_k w_{k,n}\right) \end{bmatrix}^T \begin{bmatrix} \alpha_1 \\ \vdots \\ \alpha_K \end{bmatrix} \\
&= \begin{bmatrix} \sqrt{p_1 N} + \sigma(\theta_1, \phi_1) \\ \vdots \\ \sqrt{p_K N} + \sigma(\theta_K, \phi_K) \end{bmatrix}^T \begin{bmatrix} \alpha_1 \\ \vdots \\ \alpha_k \end{bmatrix},
\end{aligned} \tag{8}
$$

where $\sigma(\theta_k, \phi_k) = \sum_n \gamma_{n,k} \cdot (\sum_{i \neq k} w_{i,n})$ represents the summed effects of interfering patterns of the other paths ($i \neq k$ and $i \in [1, K]$) at the (θ_k, ϕ_k) direction. Generally speaking, $\sigma(\theta_k, \phi_k)$ approaches 0 when the angle separation between (θ_k, ϕ_k) and (θ_i, ϕ_i) (for $i \neq k$ and $i \in [1, K]$) is large or the main beamwidth of the UCA is small. In the ideal case, with pencil-beam pattern for the main beam, $\sigma(\theta_k, \phi_k)$ approaches 0 for $k \in [1, K]$. Note that sidelobes can be suppressed by applying appropriate windowing functions for the UCA as well.

For multibeam steering, we also need to determine how the total transmit power p is distributed for the multiple beams. $\sigma(\theta_k, \phi_k) = 0$ for $k \in [1, K]$ is assumed for the discussion on power allocation schemes below, for the sake of simplicity:

(1) Uniform power allocation. Power can be uniformly distributed over all beams (i.e., $p_k = p/K$ for $k \in [1, K]$). The channel gain can be expressed in decibels, according to (8), as

$$g_u = 10 \cdot \log_{10}\left(N \cdot p \cdot \frac{\left(\sum_k a_k\right)^2}{K}\right). \tag{9}$$

(2) Nonuniform power allocation. When power is allocated to each beam proportional to the corresponding path gain (i.e., $p_k = \alpha_k^2/\sum_k \alpha_k^2$), according to (8), we have

$$g_n = 10 \cdot \log_{10}\left(N \cdot p \cdot \sum_k a_k^2\right). \tag{10}$$

The nonuniform power allocation scheme clearly outperforms the uniform one, where equality is achieved when all paths have the same gain, according to the Cauchy–Schwarz inequality. The same conclusion was drawn in [6], though mathematical explanation was missing. The uniform power allocation scheme might be useful, when only path angle information is available and path gain information is not known beforehand.

Utilizing the RT-assisted beamforming, the weights in (7) can be obtained from the power angle spectrum predicted by the RT simulations

$$\widehat{w}_{k,n} = \sqrt{\frac{\widehat{p}_k}{N}}\exp\left(j2\pi f \frac{r}{c}\sin\left(\widehat{\theta}_k\right)\cos\left(\widehat{\phi}_k - \phi_n\right)\right), \tag{11}$$

where $(\widehat{\theta}_k, \widehat{\phi}_k)$ is the RT-predicted angle for the kth path and $\widehat{p}_k$ is the power allocated to the kth path calculated from the RT-predicted gain, according to (9) or (10). Replacing $w_{k,n}$ by $\widehat{w}_{k,n}$ in (8), the channel gain $\widehat{H}_{UCA}$ achieved by RT-assisted beamforming can be calculated as

$$\widehat{H}_{UCA} = \begin{bmatrix} \sum_k \widehat{w}_{k,1} \\ \vdots \\ \sum_k \widehat{w}_{k,N} \end{bmatrix}^T \cdot \begin{bmatrix} \gamma_{1,1} & \cdots & \gamma_{1,K} \\ \vdots & \ddots & \vdots \\ \gamma_{N,1} & \cdots & \gamma_{N,K} \end{bmatrix} \begin{bmatrix} \alpha_1 \\ \vdots \\ \alpha_k \end{bmatrix}. \tag{12}$$

From (12), we can see that how well RT-assisted beamforming performs (i.e., how well $\widehat{H}_{UCA}$ approaches H_{UCA}) depends on how accurate the power angle spectrum is predicted in RT simulations. Note that the discussion is limited to UCAs in the paper, although the discussions are applicable to arbitrary array configurations. Furthermore, the analysis in the paper is limited to a 2-dimensional (2D) multipath environment (i.e., $\theta_k = 90°$ for $k \in [1, K]$) due to the limitation of measurement setting. The discussions and algorithms can be readily extended to 3D scenarios.

3. Measurement and RT Simulation

In this section, an extensive multidimensional analysis of the measured and RT-simulated channels is performed. The main contribution lies in the comprehensive comparison between measured and RT-simulated channel models in two widely different indoor propagation scenarios at 28–30 GHz.

3.1. Scenarios. Two indoor measurement scenarios were considered: an empty basement and a typical office with furniture. The empty basement is a $7.7 \times 9.1 \times 3.3$ m^3 room with an open corridor, as depicted in Figure 3. Floor, ceiling, and walls are made of solid concrete, and there are three wooden doors in the corridor (not shown). Furthermore, there is a small window and a metallic radiator on the wall opposite to the corridor (not shown). One receiver (Rx) position and six separate transmitter (Tx) locations are considered, with both the line-of-sight (LOS) region (i.e., Tx position 1 to 5) and the non-LOS region (i.e., Tx position 6). A one-meter distance was selected between the Tx locations in the room and in the corridor, respectively, as shown in Figure 3. Photos of the empty basement scenario during measurement are shown in Figure 4.

The $2.9 \times 5.7 \times 2.7$ m^3 small office is furnished with desktops, chairs, computer monitors, and so on, as depicted in Figure 5. Metallic shelves and a whiteboard are mounted on the walls. There are also two windows close to the Rx position. Measurements for a total of 6 Tx positions (with a 0.4 m separation for the Tx grid) and one Rx position were recorded. Note that measurements at these locations were performed for both the LOS scenario and the obstructed LOS scenario, where a 0.42×0.42 m^2 metallic plate was placed to block the LOS path between the Rx and Tx positions. That is, a total of 12 measurements were performed for the small office scenario. Photos of the small furnished office scenario during measurement are shown in Figure 6.

3.2. Measurements. An illustration of the measurement setup is shown in Figure 7, where a vector network analyzer (VNA) equipped with a vertically polarized biconical antenna (Tx) and a vertically polarized horn antenna (Rx) was utilized.
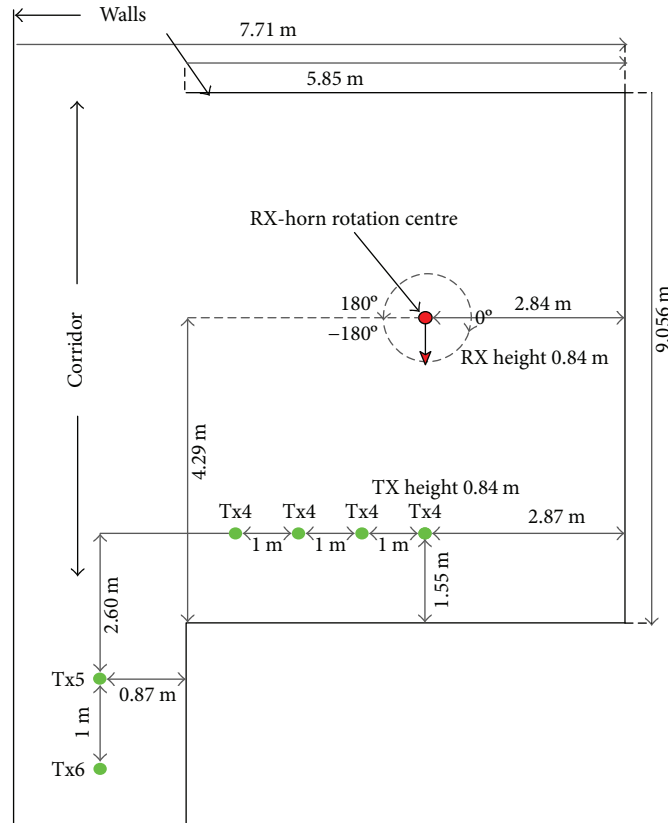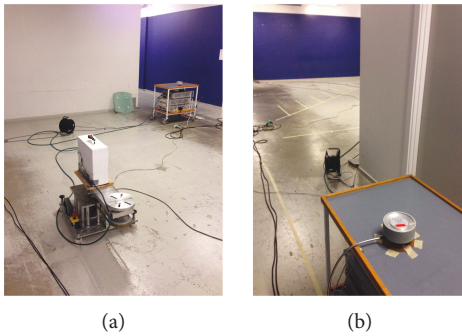
FIGURE 3: Empty basement scenario.

FIGURE 4: Photograph of the empty basement scenario: Rx view for Tx position 5 in the LOS scenario (a) and Tx view for Tx position 6 in the non-LOS scenario (b).

To avoid excessive loss and phase instability on the cable, the signal is downconverted using a reference mixer. Calibration was performed up to the antennas to eliminate the effects of Tx-Rx chain. The directive Rx antenna was rotated with 36 steps, with a step size of 10°, to cover the full azimuth plane. The Rx antenna is mounted on an automated turntable with rotations triggered by the VNA. The measurements were repeated for each Tx position. The frequency range measured is 28–30 GHz using 750 frequency points for each Rx direction. The biconical antenna has a gain of around 5.5 dB at 28–30 GHz, with a narrow beam width at around 15° half power beam width (HPBW) in the E-plane and an omnidirectional pattern in the H-plane (as shown in Figure 8(a)).
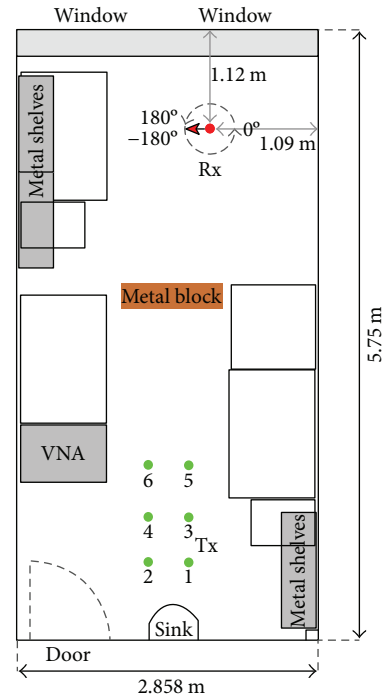

FIGURE 5: Small office scenario.

The horn antenna at 28–30 GHz has around 21° HPBW both in the H-plane and E plane, with a gain of 18.5 dBi, as shown in Figure 8(b). Note that the Tx and Rx were
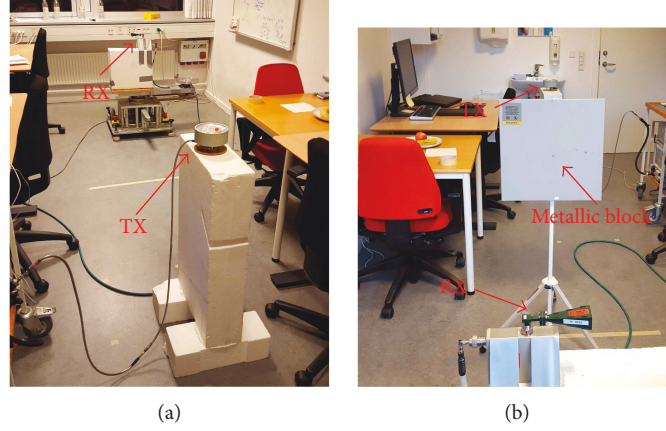
(a)　　　　　　　　　　　(b)

Figure 6: Photograph of the small office scenario: Tx view in the LOS scenario (a) and Rx view in the obstructed LOS scenario (b).
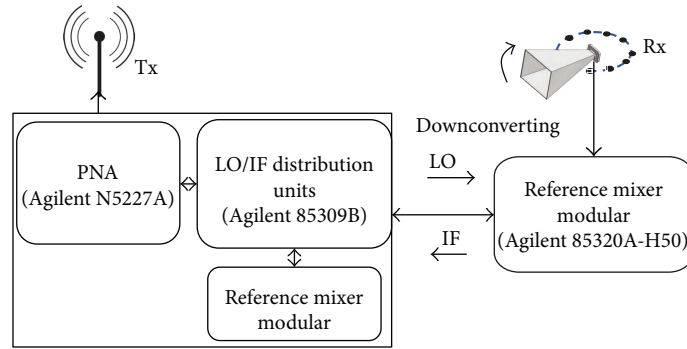

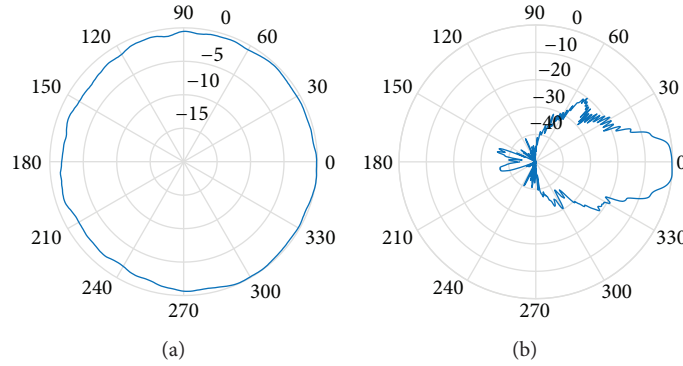Figure 7: System overview of the measurement setup.

(a)　　　　　　　　　　　(b)

Figure 8: Measured radiation pattern of the biconical antenna (a) and horn antenna (b) in the H-plane at 28–30 GHz. The measured antenna pattern of the biconical antenna is quasiomnidirectional, with a maximum deviation of 2.1 dB.

placed at the same height for both measurement scenarios, with 0.81 m for the empty basement and 0.91 m for the small office, respectively.

3.3. RT Simulations. A 3D RT tool "3D Scat", implemented by Bologna University, was used in this investigation [20]. In addition to reflection, diffraction, and transmission, the tool includes diffuse scattering adopting the effective roughness model [21]. Simplified descriptions of the scenarios have been modeled in the RT tool. The large empty room is largely simplified, where only walls, ceiling, and floor made from concrete are modeled, while small details such as a metallic

radiator, wooden doors, and a window are not included. The small office was modeled with great details, walls, ceiling, floor, and windows, as well as wooden desktops, whiteboards, and metallic shelves. Smaller objects, for example, chairs, keyboards, books, and curtains, however, are not included due to modeling complexity. Suitable material properties (i.e., permittivity and conductivity values), assumed constant over frequency band, are set to the database elements.

The 3D RT tool models typically deterministic propagation mechanisms, that is, free space propagation, transmission, reflection, and diffraction both from lateral walls or

edges, diffuse scattering due to building wall roughness or irregularities. One or several Tx can be defined, which are characterized by their positions, antenna radiation characteristics, frequency of operation, and transmit power. Similarly, one or several Rx can be defined according to their positions and antenna radiation characteristics. Then, a combination of image RT and diffuse scattering is used to simulate the rays departing from each Tx and arriving to each Rx. The computation complexity of the tool can be scaled via limiting the maximum number of interactions and the minimum power of a single ray.

RT simulation in this section has been performed with a maximum of 6 interactions including transmission, where up to six reflections, two diffraction, three reflections after scattering, one diffraction after scattering, and five total numbers of reflections and diffraction combined are further specified for each ray. This combination and number of interactions are set high to get a very detailed simulation for comparison with the measured channel. In the RT simulation, diffuse scattering is modeled using the single-lobe directive scattering model [20]. The optimal scattering parameter $S = 0.5$ was found by simulating multiple values of S and comparing the simulated results with the measured results for the best match. The optimization of S was done with respect to total power and not towards delay and angle spread. The simulation frequency is set to 29 GHz. The measured H-radiation patterns of the Tx and Rx antennas are embedded in the RT simulation data. Note that deviations between the RT simulations and measurements can be introduced by the inaccurate antenna patterns. Moreover, a limited delay resolution due to 2 GHz bandwidth, the same as in the measurement, is introduced in the RT simulation.

3.4. Data Analysis

3.4.1. Channel Analysis. The measured channel impulse response (CIR) $h^m(\tau, \phi_l)$ for each rotation angle ϕ_l (with $l = [1, \ldots, L]$) can be calculated via inverse Fourier transform of the channel frequency response directly recorded in the measurements. As for the RT simulations, the directional CIR $h^s(\tau, \phi)$ is directly available. The following channel parameters are assessed to measure how well the RT-simulated channels follow the measured channels. Note that a 35 dB power dynamic range is applied to remove weak paths both in measurements and simulations.

(1) Total Received Power. The wideband-relative received power in decibels for each Tx position can be calculated as

$$P_r = 10 \log_{10} \left(\sum_\phi \sum_\tau |h(\tau, \phi)|^2 \right), \quad (13)$$

where $h(\tau, \phi)$ can be the measured or simulated CIR.

(2) Delay Domain. To assess the delay profiles, the mean delay $\bar{\tau}$ and root mean square (RMS) delay spread σ_τ can be computed from the measured or simulated CIRs as

$$\bar{\tau} = \frac{\sum_k \tau_k \cdot \sum_\phi |h(\tau_k, \phi)|^2}{\sum_k \sum_\phi |h(\tau_k, \phi)|^2},$$

$$\sigma_\tau = \sqrt{\frac{\sum_k \tau_k^2 \cdot \sum_\phi |h(\tau_k, \phi)|^2}{\sum_k \sum_\phi |h(\tau_k, \phi)|^2} - \bar{\tau}}. \quad (14)$$

(3) Angle Domain. The circular angle spread σ_ϕ and mean $\bar{\phi}$ can be calulated, as defined in [22], to evaluate the angle domain:

$$\sigma_\phi = \min_\Delta \sigma_\phi(\Delta) = \sqrt{\frac{\sum_i \phi_{i,\mu}(\Delta)^2 \cdot \sum_\tau |h(\tau, \phi_i)|^2}{\sum_i \sum_\tau |h(\tau, \phi_i)|^2}}, \quad (15)$$

where $\phi_{i,\mu}(\Delta)$ is defined as

$$\phi_{i,u}(\Delta) = \begin{cases} 2\pi + \left(\phi_i(\Delta) - \bar{\phi}(\Delta)\right), & \text{if } \left(\phi_i(\Delta) - \bar{\phi}(\Delta)\right) < -\pi, \\ \left(\phi_i(\Delta) - \bar{\phi}(\Delta)\right), & \text{if } \left(\phi_i(\Delta) - \bar{\phi}(\Delta)\right) \leq \pi, \\ 2\pi - \left(\phi_i(\Delta) - \bar{\phi}(\Delta)\right), & \text{if } \left(\phi_i(\Delta) - \bar{\phi}(\Delta)\right) > \pi. \end{cases} \quad (16)$$

$\bar{\phi}(\Delta)$ is defined as

$$\bar{\phi}(\Delta) = \frac{\sum_i \phi_i(\Delta) \cdot \sum_\tau |h(\tau, \phi_i)|^2}{\sum_i \sum_\tau |h(\tau, \phi_i)|^2}, \quad (17)$$

and $\phi_i(\Delta) = \phi_i + \Delta$.

3.5. Comparison Results

3.5.1. Basement Scenario. The simulated power-angle-delay profiles generally match well with the measured ones for all Tx positions. The measured and RT-simulated power-angle-delay profiles for Tx position 4 are shown in Figure 9, as an example for the LOS region. As we can see in Figure 9, almost all dominant multipath components within the 35 dB dynamic range in the measured profile can be accurately predicted by the RT simulation in terms of power values, delays, and angles, with only a few exceptions of the weak multipath components. Both the measured and simulated profiles are sparse in angle and delay domains, with a dominant LOS component. The ray trajectories from RT simulation for Tx position 4 are shown in Figure 10, with dominant rays numbered in Figures 9 and 10. As seen in Figure 10, the 35 dB dynamic range in this scenario limits the interactions to maximum second order specular reflections and first order diffuse scattering. Note that the same ray trajectories were obtained based on the measured power-angle-delay profile and room geometry.

The measured and RT-simulated power-angle-delay profiles for Tx position 6 are shown in Figure 11, as an example for the non-LOS region. Though up to three clusters (group of rays with similar angles and delays) can be identified, the power-delay-angle profile is still quite sparse, with only some dominant components. An excellent agreement between RT simulation and measurement is achieved, where clusters with
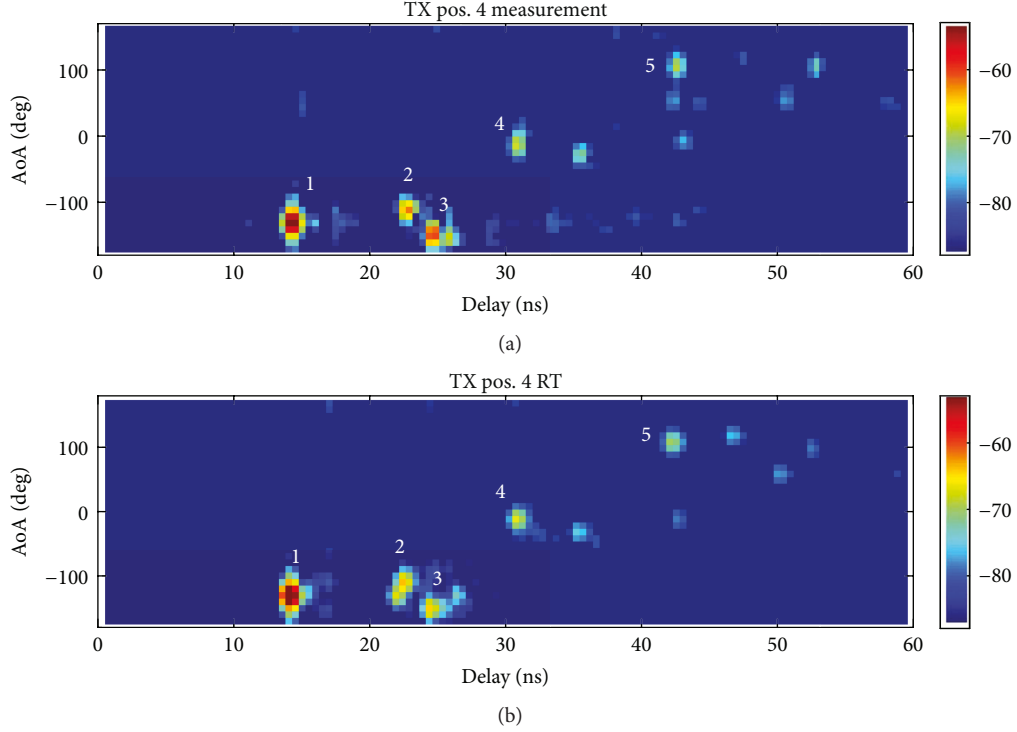
(a)

(b)

FIGURE 9: Measured (a) and RT-simulated (b) power-angle-delay profile for Tx position 4 in the basement scenario. Note that all identified multipath components are present within the 60 ns delay range in the LOS region.
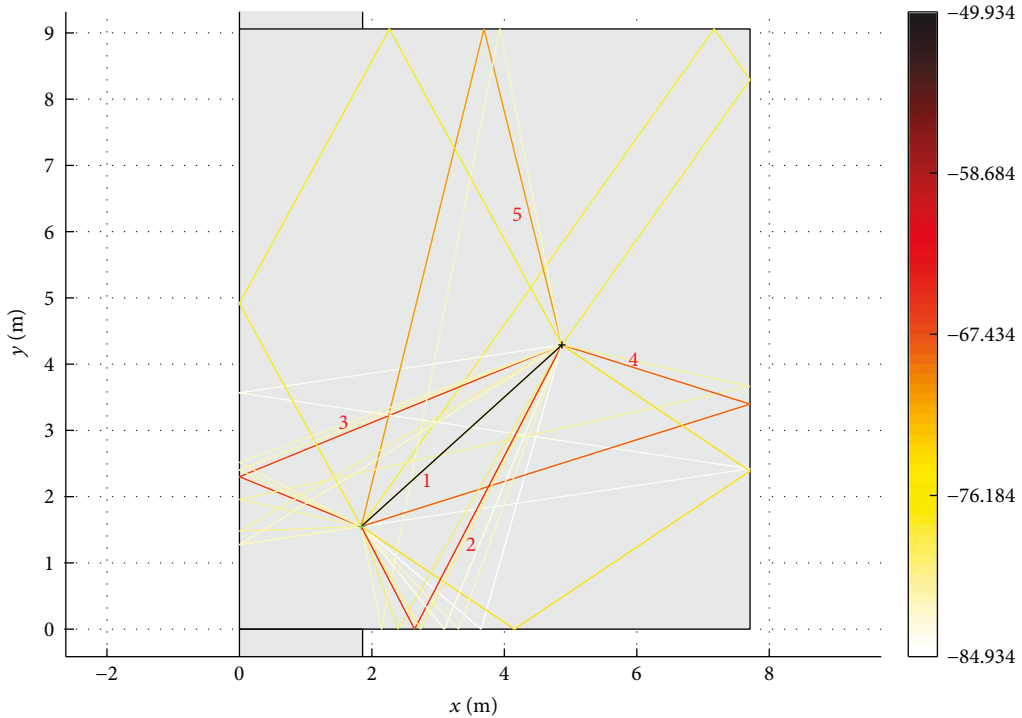

FIGURE 10: Ray trajectories of the multipath components for Tx position 4 in the basement scenario.

similar power, delays, and angles are identified. However, many more weak paths are not identified in RT results, compared to the LOS scenario, for example, Tx position 4 shown in Figure 9.

The ray trajectories from RT simulation for Tx position 6 are shown in Figure 12. The paths within the first and second clusters are spread in delay domain and constraint in angle domain due to reflections back and forth within the corridor
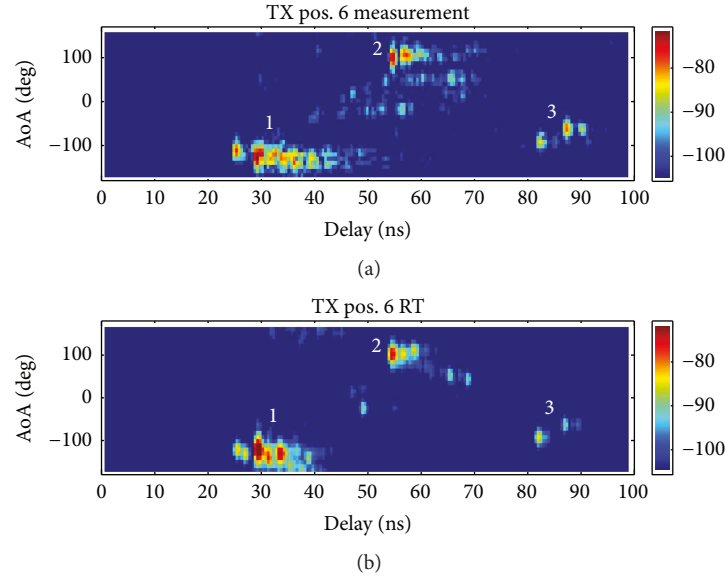
FIGURE 11: Measured (a) and RT-simulated (b) power-angle-delay profiles for Tx position 6 in the basement scenario. Note that all identified multipath components are present within the 100 ns delay range in the non-LOS region.
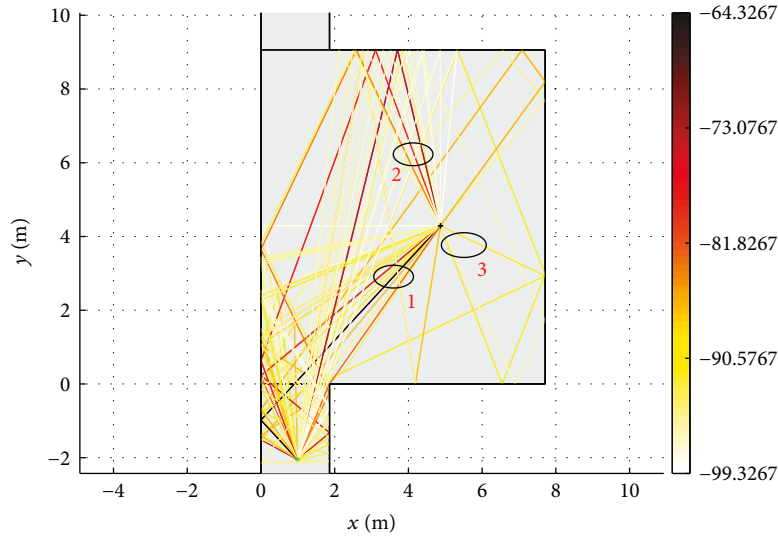

FIGURE 12: Ray trajectories of the multipath components for Tx position 6 in the basement.

before entering the room, while rays within the third cluster have different path trajectories.

To quantify how well the RT simulations predict the measurements, channel parameters, for example, total received power, delay parameters, and angle parameters, as discussed in Section 3.4.1, are analyzed. The measured total-received power and RT-simulated total-received power for all Tx positions are shown in Figure 13. The simulated power values match well with the measured ones, with a deviation of up to 2.1 dB for the LOS region (i.e., Tx position 1–5) and 3.6 dB for the non-LOS region (i.e., Tx position 6). The total received power decreases in the LOS region, as the Tx-Rx separation increases with Tx positions. The total received power is significantly

lower in TX position 6 compared to other Tx positions, as the dominant LOS component does not exist. The larger deviations in total received power for Tx position 6 are introduced by the missing weak paths in RT simulation, as shown in Figure 11.

The measured and RT-simulated delays and angle parameters are shown in Figures 14 and 15, respectively. The RT-simulated results generally underestimate the measured ones, especially for the second order statistics. A good agreement between measurements and simulations is achieved for the Tx positions in the LOS region, while a large deviation exists in the non-LOS region for both the angle and delay parameters. Within the LOS region, both mean delay $\bar{\tau}$ and mean AoA $\bar{\theta}$ are excellently predicted with the RT
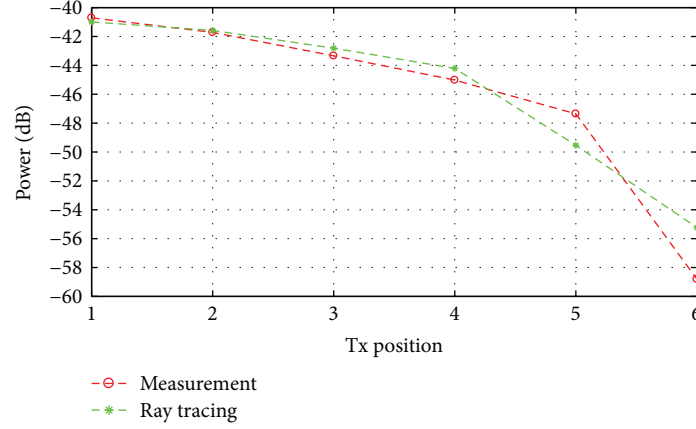
FIGURE 13: Measured and RT-simulated received power for all Tx positions for the basement scenario.

(a)   (b)
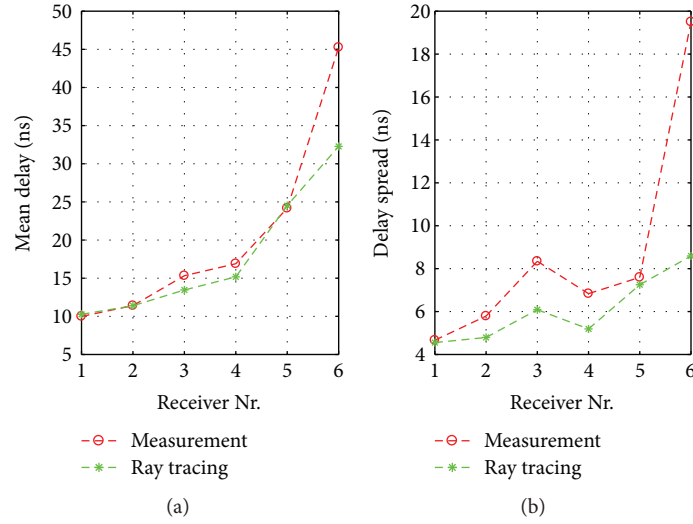
FIGURE 14: Measured and RT-simulated mean delays (a) and delay spread (b) for all Tx positions for the basement scenario.

simulation, with a deviation of up to 1.9 ns in $\bar{\tau}$ and 5.1° in $\bar{\theta}$. For the second-order statistics, delay spread σ_τ, and angle spread σ_θ, the deviations are up to 2.2 ns and 6.2°, respectively. The delay spread in the LOS region is rather small due to the dominant LOS path, with an average of around 6.6 ns measured and 5.0 ns simulated for the five Tx positions. Comparing results in the literature, 3.7 ns for a 32.9 m² and 4.8 ns for a 28.2 m² were reported in [14, 23] for 60 GHz. For the non-LOS region, the delay spread is much higher in the measurement due to the fact that many weak paths are missing in the RT simulations.

The analysis of the results in the basement scenario demonstrates that mm-wave propagation channels in an empty room (or poorly furnished) scenario can be well predicted with RT simulation for both LOS and non-LOS scenarios, with a largely simplified description of the environment. The same conclusion was drawn in [14], although the investigation was performed only for the LOS scenario at 60 GHz.

3.5.2. Small Office. It is more challenging to predict channel profiles with RT simulation in the small office scenario, compared to the empty basement scenario. The office scenario is

small in dimensions, and therefore, multiple-order interactions between rays and propagation environment are expected. Unlike the empty basement scenario, the small office is richly furnished, with many additional objects besides the walls, ceilings, and floor, for example, computer screens, chairs, metallic shelf, whiteboard, and desktops. Furthermore, various material properties corresponding to different objects, for example, concrete, glass, wood, and metal needs to be accurately modeled and calibrated as well. Moreover, many small details in the office scenario, for example, positions, shapes, and material properties of objects, are difficult to model accurately.

The same dominant multipath components can be identified in the RT simulation and measurements both for the LOS and obstructed LOS scenarios. The measured and RT-simulated power-angle-delay profiles for Tx position 1 in the office scenario are shown in Figure 16, as an example for the LOS cases. Similar to the LOS case in the basement scenario, both the measured and simulated channel profiles are sparse in angle and delay domains, with a dominant LOS component. The dominant rays are well predicted with the RT simulation. However, compared with the basement
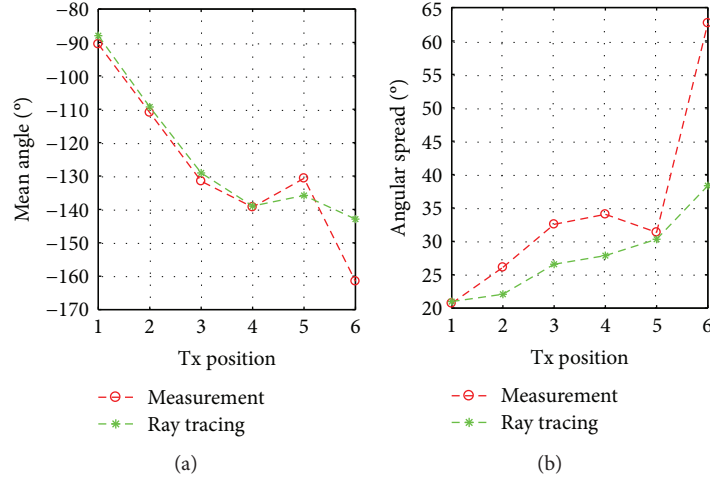
FIGURE 15: Measured and RT-simulated mean angles (a) and angle spread (b) for all Tx positions for the basement scenario.
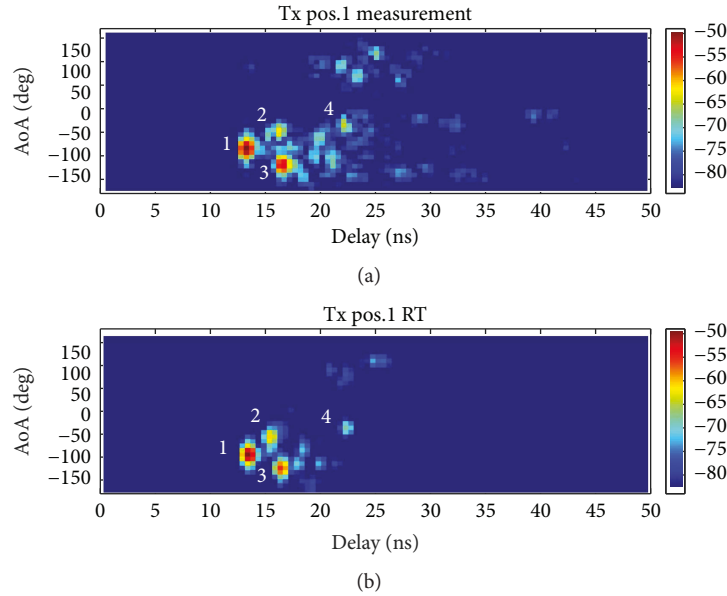

FIGURE 16: Measured (a) and RT-simulated (b) power-angle-delay profile for Tx position 1 in the small office LOS scenario.

scenario, the RT simulation fails to predict many more weak rays in the small office scenario. The ray trajectories for the Tx position 1 are shown in Figure 17(a). Four dominant rays are present, as numbered, that is, a LOS ray (ray 1) between the Rx and the Tx, two first-order-reflected rays from a whiteboard (ray 2) and a monitor (ray 3), and a second order reflected ray (ray 4). For the small office scenario, modeling furniture (e.g., monitor and whiteboard) might become important in RT simulation to predict the propagation channels, since many interactions between the rays and the objects might be present, as shown in Figures 17(a) and 17(b).

The measured and RT-simulated power-angle-delay profiles for Tx position 4 in the office scenario are shown in Figure 18, as an example for the obstructed LOS case. Though much richer multipath components are present in

the measured profile, the same dominant rays can still be identified with the RT simulation. In Figure 18, the strongest rays, numbered 1–5, are all present in the ray tracing results. The dominant rays are caused by diffraction (ray 1) and reflections (ray 2 to ray 5) inside the small office, as shown in Figure 17(b). Although delays and angles are well predicted by RT simulation for the dominant rays, the RT-simulated power fits for some paths, yet not for all of them. This is mainly due to the database simplification and material property calibration. Note that the rays identified in LOS and obstructed LOS scenarios are quite similar, except the rays impinging the Rx in LOS directions, which are blocked.

Compared to the basement scenario, larger deviations exist in channel parameters in terms of total received power, delay, and angle parameters, due to a much less richer multipath channel in the RT simulation. The measured total
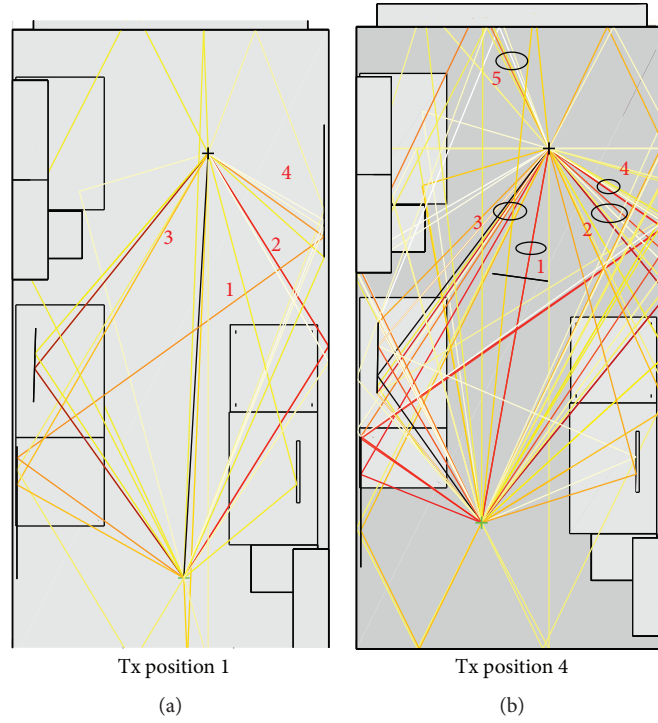
FIGURE 17: Ray trajectories of the multipath components for Tx position 1 in the LOS scenario (a) and Tx position 4 (b) in the obstructed LOS scenario in the small office.
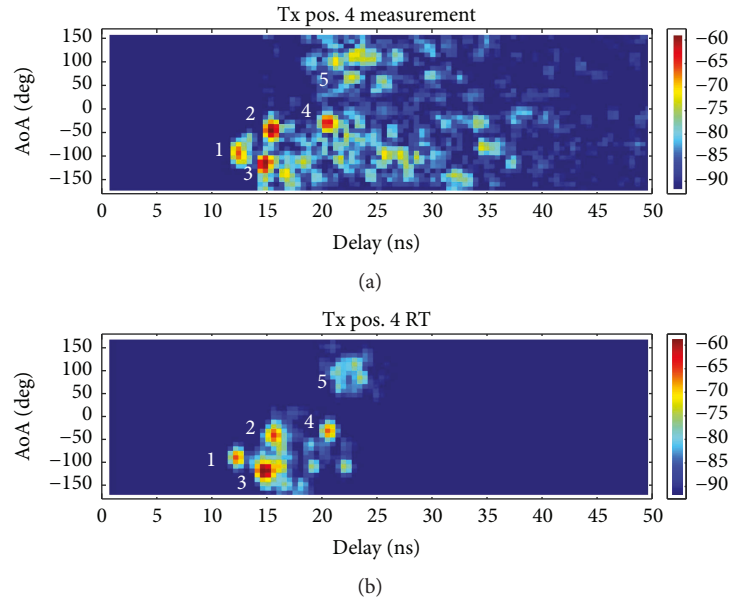

FIGURE 18: Measured (a) and RT-simulated (b) power-angle-delay profiles for Tx position 4 with the metallic plate obstructing the LOS in the small office scenario.

received power and RT-simulated total received power for all Tx positions are shown in Figure 19. Although a reasonable tendency can be observed between the measured and simulated results, the RT simulation tends to underestimate the results, due to many missing multipath components. Large deviations between the measured and simulated channels in terms of delay profiles and angle profiles exist as well due to

the many missing weak paths. In Figure 20, there are larger deviations in mean delay and delay spread compared to the empty basement scenario. This is expected as the ray tracer fails to predict many weak components after 25 ns as seen in Figures 16 and 18. As seen in Figure 21, there are some large deviations for the mean angle at position 4 and 5 and generally a 15- to 20-degree deviation in angular spread.
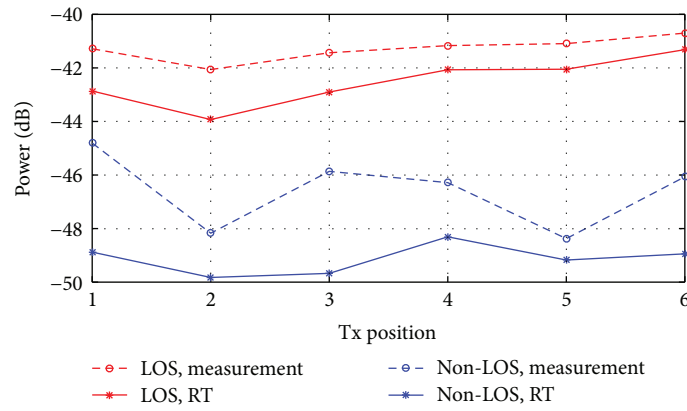
FIGURE 19: Measured and RT-simulated received power for all Tx positions for the LOS and obstructed LOS cases in the small office scenario.
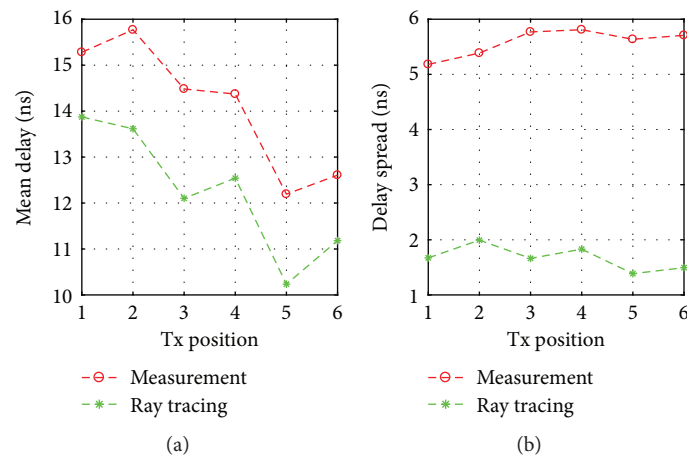

(a)

(b)

FIGURE 20: Measured and RT-simulated mean delays (a) and delay spread (b) for all Tx positions in the office LOS scenario.
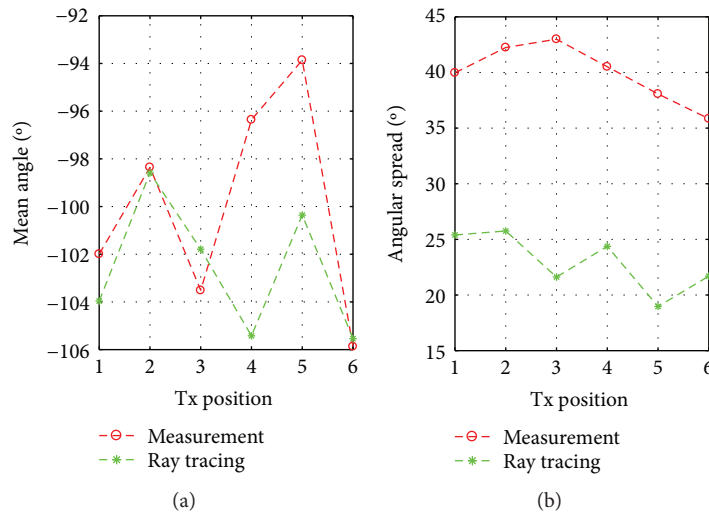

(a)

(b)

FIGURE 21: Measured and RT-simulated mean angles (a) and angle spread (b) for all Tx positions in the office LOS scenario.

The large deviation in mean angle and angle spread is mainly due to the ray tracer underestimating paths interacting with the back wall/windows in the AoA range of approximately 30 to 150 degrees. The small office is generally missing paths at larger delays in the RT predictions. Experiments in simulation settings for numbers of diffractions and scatterers as well as a higher scattering coefficient did not produce significantly better results. Increased floor and ceiling conductivity

for larger buildings, as suggested in [24], had minimal impact due to the narrow beam in elevation at both Tx and Rx. The paths are most likely missing due to the simplified model, missing model of the neighbouring rooms, or even error in material constants that impacts higher-order interactions. This mismatch contributes to a larger error in delay and angle analyses, but does not impact the estimation of dominant paths required for beamforming.

4. Performance Evaluation of RT-Assisted Beamforming

In this section, performance of the RT-assisted single-user beamforming is analyzed based on the measured and RT-simulated channels reported in Section 3. The measured and RT-simulated power angular spectra are calculated by summing up the measured and simulated power-angle-delay profiles over delay domain, respectively. For the sake of simplicity, as the measurement data is only in the azimuth plane, a UCA will be used. The array is defined with $N = 100$ isotropic antenna elements and radius $R = 7.5$ cm. The UCA offers equal angular resolution in all azimuth directions, and the high angular resolution allows us to investigate any small differences in measurement and ray tracing. The number of array elements is selected to ensure that the antenna element spacing is less than $\lambda/2$ to avoid spatial aliasing effect.

As mentioned in Section 3, the measurements sample every 10 degrees of rotation. The measured power angular profile is interpolated to a 1° interval for use in (4) and the beamforming analysis described in Section 2. The horn antenna has a 21° HPBW, and the error introduced by interpolation will be small compared to actual measurements with a horn rotation step of 1°. Similarly, the RT results are binned into 1° intervals for use in beamforming weights.

As discussed in Section 2, for the measured channels, complex weights in (7) are calculated based on the measured power angle profiles. Therefore, multiple beams are steered directly toward the target dominant directions. As for the RT-assisted beamforming case, the beams are steered towards the dominant paths predicted by the RT simulation according to (11). The channel gains H_{UCA} and $\widehat{H}_{\mathrm{UCA}}$ are obtained, respectively, as explained in Section 2.

The identified four dominant paths in the measured and simulated power angle spectra are shown in Figures 22–25 for the discussed scenarios shown in Figures 9, 11, 16, and 18, respectively. The identified dominant paths are numbered as well, according to the figures shown in Section 3. Although most paths in the measured power angle profiles are accurately predicted by the RT simulation, deviations exist in the angles and power values for some paths. As shown in the figures, multiple beams are steered to the measured and simulated dominant paths, respectively. Note that nonuniform power allocation schemes (i.e., power allocated to each beam proportional to the corresponding path gain) are shown in the figures.

The target channel gain H_{UCA} and achieved channel gain $\widehat{H}_{\mathrm{UCA}}$ for different locations in the two indoor scenarios with

FIGURE 22: The identified 4 dominant paths in the measured and RT-simulated channels and the associated multiple beams for Tx position 4 in the basement scenario.
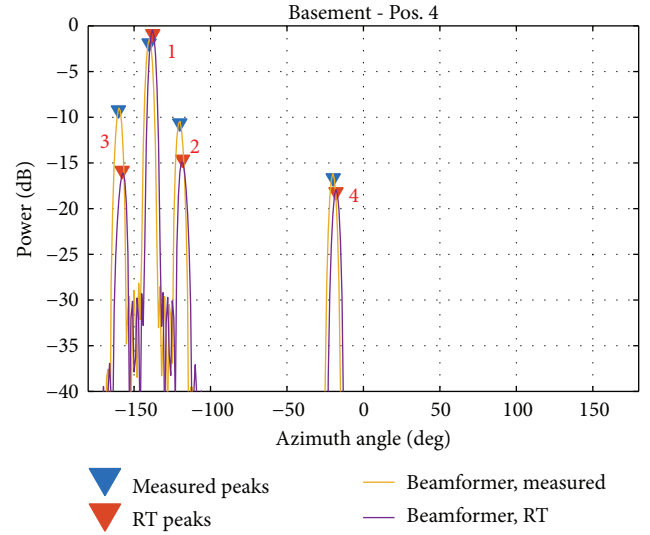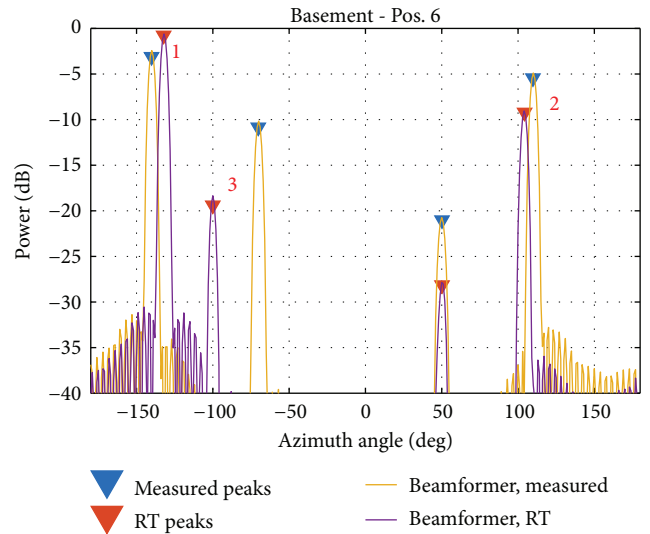

FIGURE 23: The identified 4 dominant paths in the measured and RT-simulated channels and the associated multiple beams for Tx position 6 in the basement scenario.

the uniform power allocation scheme are shown in Figure 26. For the single-beam case, only one beam was formed and steered to the most dominant path. As for the multibeam cases, 4 beams were formed and steered to the 4 most dominant paths. As explained in Section 2, with the uniform power allocation scheme, the deviation between the target and achieved channel gains are only introduced by angle prediction errors. As we can see in Figure 26, an excellent agreement is achieved for the basement scenario (for both the LOS and non-LOS regions) for single-beam and multiple-beam cases. This is expected, as the angles are accurately predicted for the basement scenarios, as explained in Section 3 and shown in Figures 22 and 23, respectively. For the office scenarios, good agreement is achieved as well both for the LOS
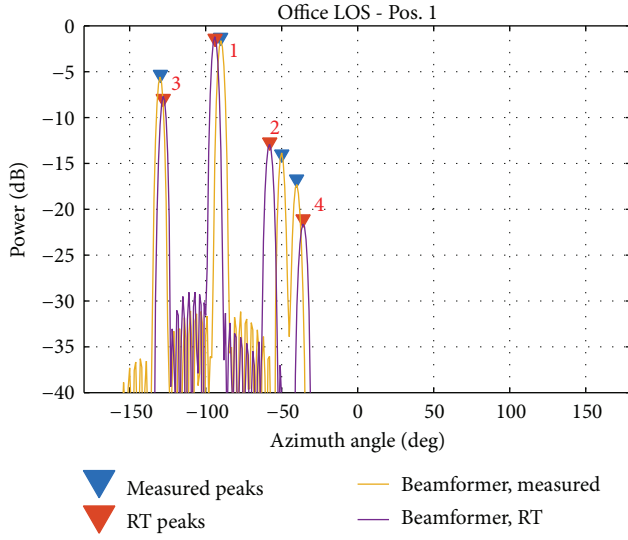
FIGURE 24: The identified 4 dominant paths in the measured and RT-simulated channels and the associated multiple beams for Tx position 1 in the office scenario.
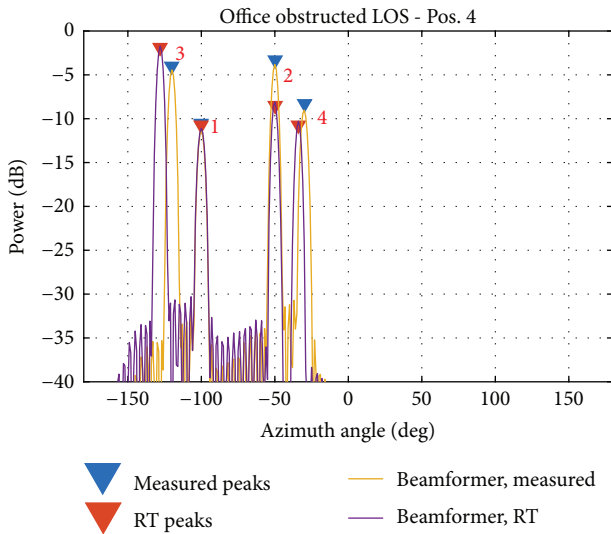

FIGURE 25: The identified 4 dominant paths in the measured and RT-simulated channels and the associated multiple beams for Tx position 4 with the metallic plate in the office scenario.
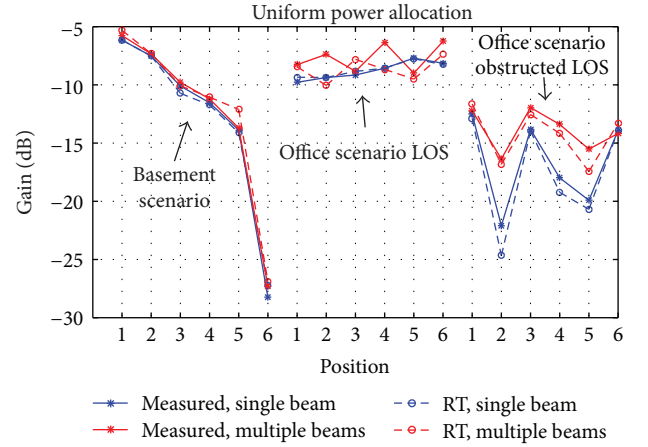

FIGURE 26: The target and achieved channel gains with the RT-assisted beamforming techniques with the uniform power allocation scheme.

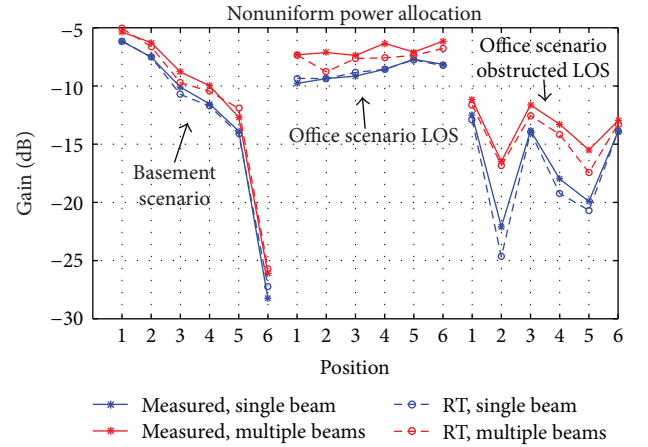FIGURE 27: The target and achieved channel gains with the RT-assisted beamforming techniques with the nonuniform power allocation scheme.

and obstructed LOS scenarios, with a deviation of up to around 3 dB. This is due to the fact that dominant paths are well predicted for the office scenario with RT tools. Furthermore, with uniform power allocation, it is expected that channel gains achieved with multibeams are dependent on the measured power at the predicted angles, more specifically, the difference in measured power between the four predicted paths. A very large power difference between the strongest and the remaining paths would indicate that power allocated to the weaker paths would be wasted with uniform allocation, while smaller differences in power values would result in similar performance or even a gain compared to single beam performance.

Both the office and basement locations typically have either similar or higher performance using the multibeam compared to the single beam. The basement has the largest difference between the strongest and remaining paths, but not significant enough for the single beam to outperform the multibeam with uniform power allocation. The small office has smaller difference in power between the dominant paths, where the largest gain is achieved by utilizing multiple beams. There are a few cases in which the RT gain is higher than that of the measured one, as seen in Figure 26 for basement position 5 and office LOS position 3. In these cases, two RT-predicted paths lines up with the same angle but different delays, effectively steering two beams towards the same direction. Whereas there is only one beam in the same direction for the measured case.

The target channel gain H_{UCA} and achieved channel gain $\widehat{H}_{UCA}$ with the nonuniform power allocation scheme are shown in Figure 27. Generally, multiple beamforming outperforms the single beamforming with the nonuniform

power allocation scheme, as expected. A performance improvement of up to 5 dB is observed for the multibeam strategy in the obstructed LOS case in the office scenario compared to the single-beam strategy. With the nonuniform power allocation scheme, the deviation between target and achieved channel gains is caused both by the angle and power prediction errors. An excellent agreement is achieved between the target and achieved channel gains, as shown in Figure 27.

There is a concern that the RT-assisted beamformer might fail in practice, since the RT simulation accuracy is highly influenced by the simulation settings and database accuracy. The mm-wave channels are expected to be more specular, compared with those at lower frequencies, as reported in the literature. Furthermore, the beams are steered towards dominant paths which are typically specular, thus reducing the need for extremely detailed maps. In this paper, we aim to investigate whether the RT-assisted beamformer is feasible in different propagation scenarios. As shown in Section 3, the ray tracing accuracy is much higher in the empty basement compared to the furnished office, but the prediction of dominant paths is accurate in both scenarios, resulting in good beamforming performance for both measured and simulated results.

5. Conclusion

In this paper, extensive channel sounding measurements and ray tracing simulations in various locations in two widely different indoor scenarios were performed at 28–30 GHz, and the channel profiles were analyzed and compared. We showed that excellent agreement can be achieved between the measured and simulated channel profiles for both LOS and non-LOS cases in the poorly furnished basement scenario. As for the small office scenario, same dominant multipath components can be identified in the RT simulation and measurements, while many weak path components were missing in the ray tracing simulations. We further investigated the feasibility of ray tracing-assisted beamforming, based on the measured and simulated channel profiles. Single beamforming and multibeamforming are investigated with different power allocation schemes. We showed that ray tracing-assisted beamforming can be reliably used in the two indoor scenarios, since an excellent agreement is achieved between the ray tracing result and the target.

Conflicts of Interest

The authors declare that there is no conflict of interest regarding the publication of this paper.

Acknowledgments

References

[1] S. Salous, V. D. Esposti, F. Fuschini et al., "Millimeter-wave propagation: characterization and modeling toward fifth-generation systems. [wireless corner]," *IEEE Antennas and Propagation Magazine*, vol. 58, no. 6, pp. 115–127, 2016.

[2] Y. Niu, Y. Li, D. Jin, L. Su, and A. V. Vasilakos, "A survey of millimeter wave communications (mmWave) for 5G: opportunities and challenges," *Wireless Networks*, vol. 21, no. 8, pp. 2657–2676, 2015.

[3] 3GPP TR 38.900, "Channel model for frequency spectrum above 6 GHz," 2016.

[4] W. Roh, J. Y. Seol, J. Park et al., "Millimeter-wave beamforming as an enabling technology for 5G cellular communications: theoretical feasibility and prototype results," *IEEE Communications Magazine*, vol. 52, no. 2, pp. 106–113, 2014.

[5] S. Sun, T. S. Rappaport, R. W. Heath, A. Nix, and S. Rangan, "MIMO for millimeter-wave wireless communications: beamforming, spatial multiplexing, or both?," *IEEE Communications Magazine*, vol. 52, no. 12, pp. 110–121, 2014.

[6] V. Degli-Esposti, F. Fuschini, E. M. Vitucci et al., "Ray-tracing-based mm-wave beamforming assessment," *IEEE Access*, vol. 2, pp. 1314–1325, 2014.

[7] V. Degli-Esposti, F. Fuschini, E. M. Vitucci et al., "Polarimetric analysis of mm-wave propagation for advanced beamforming applications," in *2015 9th European Conference on Antennas and Propagation (EuCAP)*, pp. 1–4, Lisbon, Portugal, 2015.

[8] Aalto University, AT&T, BUPT et al., "White paper: 5G Channel Model for bands up to 100 GHz," 2016, http://www.5gworkshops.com/5GCM.html.

[9] S. Salous, "COST IC1004 white paper on channel measurements and modeling for 5G networks in the frequency bands above 6 GHz," 2016.

[10] F. Fuschini, H. El-Sallabi, V. Degli-Esposti, L. Vuokko, D. Guiducci, and P. Vainikainen, "Analysis of multipath propagation in urban environment through multidimensional measurements and advanced ray tracing simulation," *IEEE Transactions on Antennas and Propagation*, vol. 56, no. 3, pp. 848–857, 2008.

[11] J. Medbo, K. Börner, K. Haneda et al., "Channel modelling for the fifth generation mobile communications," in *The 8th European Conference on Antennas and Propagation (EuCAP 2014)*, pp. 219–223, The Hague, Netherlands, 2014.

[12] M. Peter, W. Keusgen, and R. Felbecker, "Measurement and ray-tracing simulation of the 60 GHz indoor broadband channel: model accuracy and parameterization," in *The 2nd European Conference on Antennas and Propagation, (EuCAP 2007)*, pp. 1–8, Edinburgh, UK, 2007.

[13] J. Pascual-García, J. M. Molina-García-Pardo, M. T. Martínez-Inglés, J. V. Rodríguez, and N. Saurín-Serrano, "On the importance of diffuse scattering model parameterization in indoor wireless channels at mm-wave frequencies," *IEEE Access*, vol. 4, pp. 688–701, 2016.

[14] M. T. Martinez-Ingles, D. P. Gaillot, J. Pascual-Garcia, J. M. Molina-Garcia-Pardo, M. Lienard, and J. V. Rodriguez, "Deterministic and experimental indoor mmW channel modeling," *IEEE Antennas and Wireless Propagation Letters*, vol. 13, pp. 1047–1050, 2014.

[15] D. Dupleich, F. Fuschini, R. Mueller et al., "Directional characterization of the 60 GHz indoor-office channel," in *2014 XXXIth URSI General Assembly and Scientific Symposium (URSI GASS)*, pp. 1–4, Beijing, China, 2014.

[16] N. Zhang, J. Dou, L. Tian et al., "Dynamic channel modeling for an indoor scenario at 23.5 GHz," *IEEE Access*, vol. 3, pp. 2950–2958, 2015.

[17] J. Dou, L. Tian, H. Wang, X. Yuan, N. Zhang, and S. Mei, "45GHz propagation channel modeling for an indoor conference scenario," in *2015 IEEE 26th Annual International Symposium on Personal, Indoor, and Mobile Radio Communications (PIMRC)*, pp. 2225–2228, Hong Kong, China, 2015.

[18] E. Perahia, C. Cordeiro, M. Park, and L. L. Yang, "IEEE 802.11 ad: defining the next generation multi-Gbps wi-fi," in *2010 7th IEEE Consumer Communications and Networking Conference*, pp. 1–5, Las Vegas, NV, USA, 2010.

[19] M. Dong, W. M. Chan, T. Kim, K. Liu, H. Huang, and G. Wang, "Simulation study on millimeter wave 3D beamforming systems in urban outdoor multi-cell scenarios using 3D ray tracing," in *2015 IEEE 26th Annual International Symposium on Personal, Indoor, and Mobile Radio Communications (PIMRC)*, pp. 2265–2270, Hong Kong, China, 2015.

[20] V. Degli-Esposti, D. Guiducci, A. de'Marsi, P. Azzi, and F. Fuschini, "An advanced field prediction model including diffuse scattering," *IEEE Transactions on Antennas and Propagation*, vol. 52, no. 7, pp. 1717–1728, 2004.

[21] V. Degli-Esposti, F. Fuschini, E. M. Vitucci, and G. Falciasecca, "Measurement and modelling of scattering from buildings," *IEEE Transactions on Antennas and Propagation*, vol. 55, no. 1, pp. 143–153, 2007.

[22] 22GPP TR 25.996, "Spatial channel model for multiple input multiple output (mimo) simulations," 2009.

[23] W. Fu, J. Hu, and S. Zhang, "Frequency-domain measurement of 60 GHz indoor channels: a measurement setup, literature data, and analysis," *IEEE Instrumentation Measurement Magazine*, vol. 16, no. 2, pp. 34–40, 2013.

[24] E. M. Vitucci, F. Fuschini, and V. Degli-Esposti, "Ray tracing simulation of the radio channel time-and angle-dispersion in large indoor environments," in *The 8th European Conference on Antennas and Propagation (EuCAP 2014)*, pp. 1771–1774, The Hague, Netherlands, 2014.